3D-Printed Metal–Organic Framework-Derived Composites for Enhanced Photocatalytic Hydrogen Generation

Hussain, Mian Zahid; Großmann, Paula F.; Kohler, Fabian; Kratky, Tim; Kronthaler, Laura; van der Linden, Bart; Rodewald, Katia; Rieger, Bernhard; Fischer, Roland A.; Xia, Yongde

DOI
10.1002/solr.202200552

Publication date
2022

Document Version
Final published version

Published in
Solar RRL

Citation (APA)
Hussain, M. Z., Großmann, P. F., Kohler, F., Kratky, T., Kronthaler, L., van der Linden, B., Rodewald, K., Rieger, B., Fischer, R. A., & Xia, Y. (2022). 3D-Printed Metal–Organic Framework-Derived Composites for Enhanced Photocatalytic Hydrogen Generation. *Solar RRL*, *6*(10), Article 2200552. https://doi.org/10.1002/solr.202200552

Solar RRL
www.solar-rrl.com

3D-Printed Metal–Organic Framework-Derived Composites for Enhanced Photocatalytic Hydrogen Generation

Mian Zahid Hussain, Paula F. Großmann, Fabian Kohler, Tim Kratky, Laura Kronthaler, Bart van der Linden, Katia Rodewald, Bernhard Rieger, Roland A. Fischer, and Yongde Xia**

Direct ink writing technique is used to 3D print Ti-metal–organic framework (MOF) NH_2-MIL-125 mixed with boehmite dispersal. Pt is also deposited onto 3D-printed monolith using atomic layer deposition (ALD) to offer additional catalytic sites. The Ti-MOF-derived powder sample and the pyrolyzed 3D-printed monolith samples are evaluated for photocatalytic H_2 evolution under UV–vis light. As a proof of concept, herein, it is demonstrated that 3D-printed MOF-derived monolith photocatalysts show five times higher H_2 evolution performance compared with TiO_2/C powder sample due to better interaction between 3D-printed photocatalysts and the incident light. The high surface area, the formation of hierarchical macro- to nanopores, and the optimizable shape/size of the 3D-printed catalyst maximize the exposure of catalytic active sites to incident photons and increase their photocatalytic H_2 evolution performance. In addition, the N-functionalized porous carbon from organic linker, and the uniformly distributed Pt/PtO_x species deposited by ALD, provide cocatalytic active sites for photocatalytic reaction and further enhance photocatalytic activity 30% of 3D-printed monoliths. This work on the 3D-printed MOF-derived free-standing monoliths for photocatalytic application provides a readily available approach to further fabricate a variety of 3D-printed MOF-based and derived materials for different energy and environment applications.

1. Introduction

One of the biggest challenges to planet Earth is the unprecedented rising of carbon emissions (estimated 410 ppm in 2020), which is the major contributor to environmental pollution and climate change.[1–3] Moreover, the increasing energy demand together with the depleting fossil fuel reserves are ringing alarms to find alternative energy resources. To deal with these global challenges, renewable energy resources are widely recognized as the most plausible options. Among numerous different available renewable energy resources, hydrogen (H_2) generated from water splitting is considered as the most green, cost-effective, and clean energy carrier and fuel.[4] It can be directly used for domestic heating, fuel cells, automobiles, and a variety of applications in industry.[5–7] Currently, majority of H_2 is produced via the methane steam reforming process which is environmentally unsustainable and economically expensive.[8,9] H_2 production via electrocatalytic water splitting has been extensively interesting and widely explored.[10–12] As an alternative, solar

M. Z. Hussain, T. Kratky, L. Kronthaler, R. A. Fischer
School of Natural Sciences and Catalysis Research Center
Technical University of Munich
Lichtenbergstr. 4, 85748 Garching, Germany
E-mail: ge68muq@tum.de

P. F. Großmann, K. Rodewald, B. Rieger
WACKER-Chair of Macromolecular Chemistry
School of Natural Sciences, Department of Chemistry and Catalysis Research Center
Technical University of Munich
Lichtenbergstr. 4, 85748 Garching, Germany

The ORCID identification number(s) for the author(s) of this article can be found under https://doi.org/10.1002/solr.202200552.

DOI: 10.1002/solr.202200552

F. Kohler
Laboratory for Biomolecular Nanotechnology
Physics Department
Technical University of Munich
Coulombwall 4a, 85748 Garching, Germany

F. Kohler
Munich Institute of Biomedical Engineering
Technical University of Munich
Boltzmannstr. 11, 85748 Garching, Germany

B. van der Linden
Catalysis Engineering
Chemical Engineering Department
Delft University of Technology
van der Maasweg, 9, 2629 HZ Delft, Netherlands

Y. Xia
College of Engineering
Mathematics and Physical Sciences
University of Exeter
Exeter EX4 4QF, United Kingdom
E-mail: y.xia@exeter.ac.uk

light-driven water splitting in the presence of suitable catalysts is a very promising approach to generate green H_2. However, the bottleneck is the high cost for the use of noble metal catalysts and the lower efficiencies when non-noble metal photocatalysts are used.[13]

Despite the availability of plenty of new materials for photocatalytic water splitting, TiO_2 is still one of the most promising photocatalysts due to its nontoxicity, natural abundance, and low cost.[14,15] Nevertheless, the wide-bandgap energy (3.2 eV for anatase TiO_2), the poor visible light absorption, the low specific surface area, the fast surface charge recombination, and the agglomeration of the particles are the major factors to limit their large-scale utilizations as efficient photocatalysts. However, the bandgap energy of TiO_2 can be readily tuned by controlled doping of cationic or anionic species to expand its light absorption capacities of TiO_2 from ultraviolet light into visible light region of the electromagnetic spectrum.[14,16,17] For a high-performing photocatalyst, charge recombination should be minimized and the catalytic active sites should be easily accessible for photocatalytic reactions.[15,18–20]

Metal–organic frameworks (MOFs) are a class of coordination polymers in which metal ions/clusters and organic linkers connect through coordination bonds to form reticular structures via a self-assembly method.[21,22] Usually they exhibit exceptionally high surface areas, tunable porosities, well-defined morphologies, and highly crystalline structures. Among them, Ti-based MOFs, such as NH_2-MIL-125(Ti), are chemically stable under ambient conditions and have demonstrated their potential to be functioning as photocatalysts.[23–26] Nonetheless, the limited electric charge generation and the poor charge transfer mechanisms make such systems less favorable to be directly employed as photocatalysts.[27,28] However, in the past few years, MOFs have been demonstrated to be ideal sacrificial templates and precursors to derive multifunctional and tunable nanocomposites, where self-doped metal or metal compound (oxide, sulfide, carbide, or phosphide, etc.) nanoparticles are embedded in (multi)functionalized porous carbon structures. Ti-MOF-derived TiO_2/C composites usually offer better catalytic performance compared to conventional TiO_2 due to the self-doped nonmetal species from organic linkers.[29–33] Such composite systems inherit high specific surface areas, tunable pores, and easily accessible catalytic active sites.

Despite the great advancement in this field, both conventional metal oxides and MOF-derived metal oxide photocatalysts are usually available in the form of powder.[5,31,34] From the application of catalysts in the industrial-scale point of view, practically, it is expensive and difficult to work with powder-based photocatalysts. Moreover, in a photoreactor, not all the powder dispersion is equally exposed to the incident solar light due to the limitations of the reactor design.[35] Therefore, the development of novel hybrid materials with optimal photocatalytic properties and practical designs is of utmost importance to obtain easy-to-handle high-performing photocatalysts. Additive manufactured catalysts such as 3D-printed MOFs based and/or derived materials can be an excellent approach to fabricate free-standing and customized catalytic materials for high performance.[36,37] Direct ink writing (DIW) technique (also called robocasting) is a readily available process which can be used to 3D print MOF-containing paste.[38,39] As a proof of concept, our study on 3D-printed Ti-MOF-derived photocatalysts for H_2 evolution from water splitting is presented in this work. It is demonstrated that under UV–vis light, H_2 evolution performance of 3D-printed Ti-MOF-derived monolith is five times higher than that of photocatalysts in the form of powder. Moreover, loading of Pt on 3D-printed monoliths via atomic layer deposition provides additional catalytic active sites, which further enhance H_2 evolution performance up to 30%. It is important to note that increasing the MOF content in the 3D-printed monolith precursor can create more catalytic active sites. Furthermore, diffusion limitations (mass transport and/or heat transfer) in H_2 evolution reaction can be minimized by optimizing the shape/size of the printed monoliths. Optimally these parameters can efficiently enhance the interaction between incident light and catalytic active sites to maximize the photocatalytic activity.[40] In contrast to powder catalysts, using shaped catalysts allows conveniently switching from (semi-)batch setups to continuous flow reaction processes. In addition, optimal pyrolysis conditions of 3D-printed MOF-derived photocatalysts also play a very crucial role in determining their photocatalytic performance for H_2 production. To the best of our knowledge, this is the first ever study on 3D-printed boehmite/Ti-MOF derived free-standing monoliths for photocatalytic application. This approach can be easily expanded to fabricate a variety of 3D-printed MOF-based or derived materials for energy and environment applications.

2. Results and Discussion

The boehmite/MOF monoliths were 3D printed by a DIW method. The grid-like structures of boehmite and boehmite/Ti-MOF with a target diameter of 10 mm and seven layers with each layer height of 0.4 mm were printed by extruding the paste through a thin nozzle (diameter 0.51 mm). The extruded paste is shear thinning, enabling a constant flow through the nozzle when pressure is applied as well as stable structures after the extrusion. As shown in Figure S1a–d, Supporting Information, after drying, the grid-like structures have an overall diameter of 9 mm and a total height of 2.7 mm. The average diameter of the extruded strand is 0.5 mm and the strand length in the printed monolithic structures is ≈61 mm. Compared with the targeted dimensions, only 90% of the overall diameter and 96% of the overall height are present after drying. Upon pyrolysis of these boehmite/Ti-MOF grids at 750 °C for 2 h under Ar atmosphere, a further small but uniform shrinkage in all dimensions was observed (Figure S1e–f, Supporting Information) due to the evaporation of organic species during the pyrolysis process. The precursor material such as boehmite was transformed into γ-Al_2O_3, whereas the Ti-MOF NH_2-MIL-125 was transformed into TiO_2/C, respectively,[19,29,31,41,42] which was confirmed by powder X-ray diffraction (PXRD).

As shown in **Figure 1**a, the overall diameter of the pyrolyzed monolith (Al_2O_3/TiO_2/Pt/C_{3DP}) was measured to be 8.4 mm with a strand diameter of 0.42 mm and the strand length of 55 mm, respectively, which suggest that pyrolyzed Al_2O_3/TiO_2/Pt/C_{3DP} monolith retains 93% of original overall diameter, 83% of strand diameter, and 90% of strand length of its 3D-printed boehmite/Ti-MOF monolith precursor. Moreover, the overall height of the pyrolyzed monolith is 2.5 mm, which accounts for 90% overall height of its precursor. In general, compared with the as-printed boehmite/Ti-MOF monoliths,

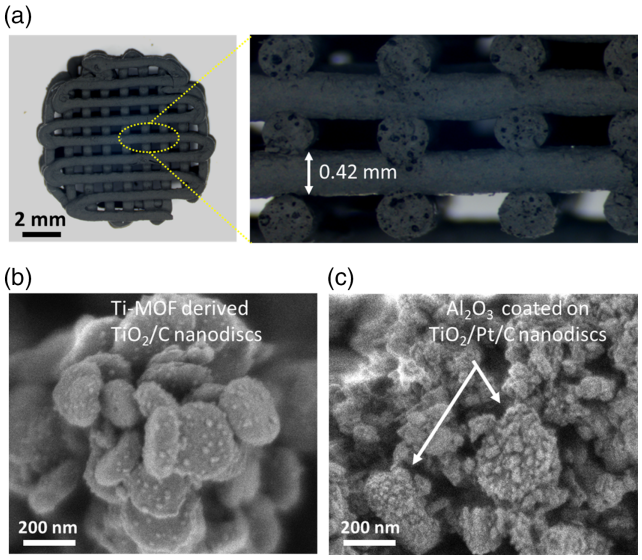

Figure 1. a) Optical image of pyrolyzed 3D-printed $Al_2O_3/TiO_2/Pt/C_{3DP}$ monolith. Right-hand enlarged image is the cross-sectional view of the monolith. SEM images of b) Ti-MOF-derived TiO_2/C_P and c) Pt-deposited boehmite/Ti-MOF-derived $Al_2O_3/TiO_2/Pt/C_{3DP}$.

10% of volume shrinkage was observed in the pyrolyzed $Al_2O_3/TiO_2/C_{3DP}$ monoliths. However, due to the slow and uniform shrinkage, the geometrical shape remained intact. As shown in Figure 1a (enlarged region), the individual strands in each printed layer of the pyrolyzed samples are stacked uniformly without showing any structural deformation. The formed macropores can be clearly observed in the pyrolyzed monoliths. The formation of hierarchical pores from micropores to macropores was confirmed by N_2 gas sorption analysis.

Scanning electron microscopy (SEM) images of the precursor boehmite/Ti-MOF paste are shown in Figure S2, Supporting Information. NH_2-MIL-125(Ti) shows disc-like morphologies with an average diameter of 500 nm (Figure S2a, Supporting Information). In boehmite/Ti-MOF paste (Figure S2b, Supporting Information), NH_2-MIL-125(Ti) is coated with small boehmite particles which are uniformly distributed throughout the sample. After pyrolysis at 750 °C for 2 h under Ar atmosphere, the average crystallite size in the derived powder sample TiO_2/C_P reduces to ≈300 nm (Figure 1b).[29] The SEM images of the pyrolyzed 3D-printed $Al_2O_3/TiO_2/C_{3DP}$ grids show that the MOF-derived TiO_2/C is uniformly covered with Al_2O_3 nanoparticles (Figure 1c).

PXRD patterns of boehmite, NH_2-MIL-125(Ti), and their mixed paste (Figure S3, Supporting Information) confirm that Ti-MOF is chemically stable after 3D printing. The signature peaks of boehmite and NH_2-MIL-125(Ti) remain intact and can be clearly observed in the boehmite/Ti-MOF paste. As shown in **Figure 2**a, after pyrolysis at 750 °C in Ar atmosphere, Ti-MOF and boehmite/Ti-MOF-derived sample TiO_2/C_P and

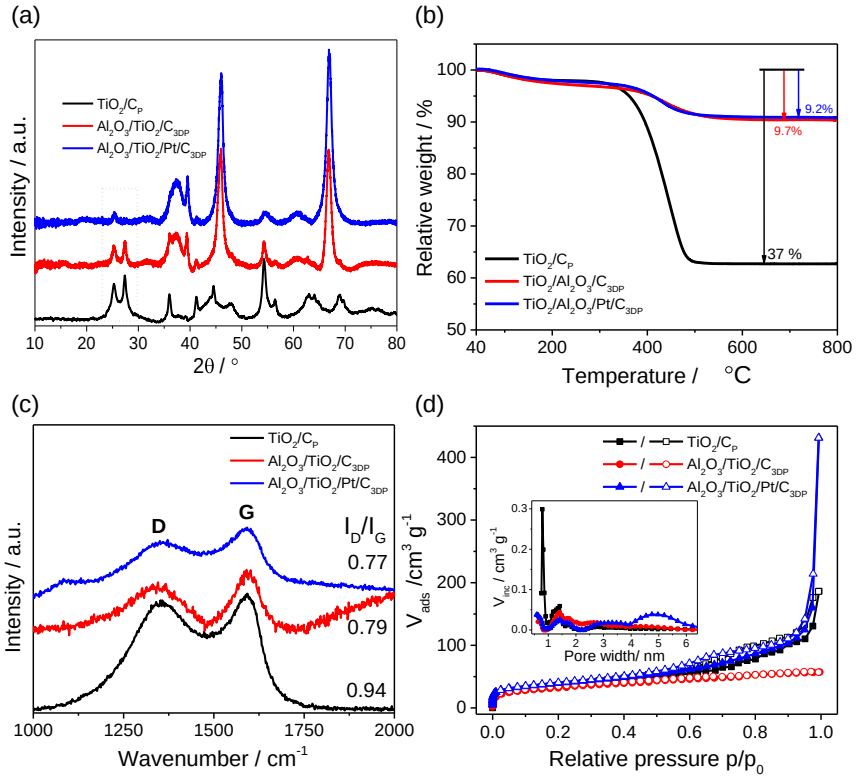

Figure 2. a) PXRD patterns, b) TGA curves under synthetic air atmosphere, c) Raman spectra, and d) N_2 sorption isotherms of Ti-MOF derived TiO_2/C_P (black) powder and 3D-printed boehmite/Ti-MOF-derived $Al_2O_3/TiO_2/C_{3DP}$ monolith (red) and $Al_2O_3/TiO_2/Pt/C_{3DP}$ monolith (blue). Inset in d) represents the PSD derived from the adsorption branch of N_2 sorption isotherms.

$Al_2O_3/TiO_2/C_{3DP}$ exhibit the diffraction peak of TiO_2 at 2θ of 25.26°, indexed to (101) of anatase, whereas this diffraction peak was shifted to 25.40° in Pt-deposited sample $Al_2O_3/TiO_2/Pt/C_{3DP}$. Moreover, the characteristic (110) peak of rutile phase of TiO_2, which appeared at around 2θ of 27.36° in Pt-free samples, almost disappeared in Pt-deposited pyrolyzed sample.[43,44] This clearly indicates that the Pt species not only chemically interact with TiO_2 and Al_2O_3 species but also influence their crystalline phases. In sample $Al_2O_3/TiO_2/C_{3DP}$, the PXRD patterns show signature peaks appearing at 2θ of 37.4°, 39.37°, 46.0°, and 66.8°, which correspond to the (311), (222), (400), and (440) planes of γ-Al_2O_3 respectively. However, in Pt-deposited samples, two additional peaks were observed at 2θ of 36.8° and 39.5° which are assigned to (210) of PtO_x and (111) of metallic Pt^0 nanoparticles respectively.[44–46] The particle sizes, chemical nature, and oxidation states of the deposited Pt, TiO_2 and γ-Al_2O_3 were further confirmed by high resolution transmission electron microscopy (HRTEM), X-ray photoelectron spectroscopy (XPS), and Raman spectroscopy.

When Ti-MOF and boehmite/Ti-MOF precursors are pyrolyzed under Ar atmosphere, it is expected that a significant amount of nitrogen-functionalized porous carbon can be formed due to the decomposition of organic linker NH_2-BDC in the Ti-MOF. Thermogravimetric analysis (TGA) was carried out to quantify the amount of carbon in these pyrolyzed samples. As shown in Figure 2b, Ti-MOF-derived TiO_2/C_P exhibited a relative weight loss of 37 wt% under synthetic air due to the oxidation of carbon and nitrogen species in the form of CO_x and NO_x, respectively. In samples $Al_2O_3/TiO_2/C_{3DP}$ and $Al_2O_3/TiO_2/Pt/C_{3DP}$, the weight loss was observed 9.7 and 9.2 wt% respectively. A small difference of 0.5 wt% in these two (otherwise identical) samples can be due to the presence of Pt in one of the samples. Obviously, the TGA curves of these pyrolyzed samples are completely different from the TGA curves of their precursor species (as-prepared Ti-MOF, boehmite dispersal, and their mixture) under the same conditions (Figure S4, Supporting Information).

To investigate the nature of Ti-MOF-derived carbon, Raman spectra were recorded. As shown in Figure 2c, D and G bands of graphitic carbon were observed at 1350 and 1590 cm^{-1} respectively in sample TiO_2/C_P. In general, D bands arise from the out-of-plane vibrations therefore correlated to defect or disordered carbon and G bands on the other hand are caused by in-plane vibrations of sp^2-bonded carbon atoms in hexagonal rings.[47,48]. The I_D/I_G ratio in this sample was calculated to be 0.94. However, in 3D-printed boehmite/Ti-MOF-derived sample $Al_2O_3/TiO_2/C_{3DP}$, the D and G bands were shifted to 1340 and 1593 cm^{-1} respectively with a I_D/I_G ratio of 0.79. It is interesting to note that in Pt-deposited sample $Al_2O_3/TiO_2/Pt/C_{3DP}$, the D and G band values were shifted to 1357 and 1589 cm^{-1} respectively and I_D/I_G was calculated to be 0.77. The higher I_D/I_G value indicates the formation of defects in graphitic carbon. A relatively higher I_D/I_G value in sample TiO_2/C_P is due to the presence of higher N species in porous carbon.[14,16,18,42,49,50] However, in 3D-printed boehmite/Ti-MOF-derived $Al_2O_3/TiO_2/C_{3DP}$ and $Al_2O_3/TiO_2/Pt/C_{3DP}$ samples, the relatively lower I_D/I_G value can be attributed to the lower amount of N species on carbon. This is likely as less heat can be transferred into the carbon due to the presence of Al_2O_3 on the carbon, which results in less surface defects in such carbon.[29,47,49]

The Brunauer–Emmett–Teller (BET) surface area and pore size distribution (PSD) of the 3D-printed boehmite/Ti-MOF (precursors) and their derived composites were recorded. As shown in Figure S5, Supporting Information, the specific surface areas (SSAs) of activated Ti-MOF, boehmite, and boehmite/Ti-MOF are 1460, 98.4, and 363 $m^2 g^{-1}$ respectively. It can be clearly seen

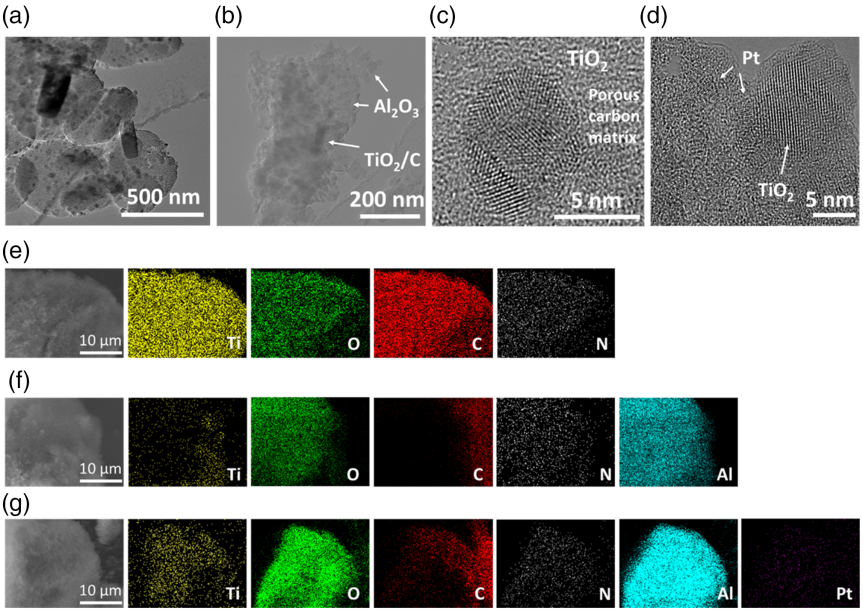

Figure 3. TEM images of a) TiO_2/C_P and b) $Al_2O_3/TiO_2/C_{3DP}$. HRTEM images of c) $Al_2O_3/TiO_2/C_{3DP}$ and d) $Al_2O_3/TiO_2/Pt/C_{3DP}$. EDX elemental mappings of e) TiO_2/C_P, f) $Al_2O_3/TiO_2/C_{3DP}$, and g) $Al_2O_3/TiO_2/Pt/C_{3DP}$. Color codes for each element are Ti: yellow; O: green: C: red; N: grey; Al: cyan; and Pt: magenta.

that in boehmite/MOF paste, due to the presence of 30 wt% of Ti-MOF, this printed monolith has higher amount of micropores with pore diameter of 0.7 nm that originates from the pure MOF. Moreover, a small amount of relatively larger pores of 1.4 nm are also presented in both samples. In 3D-printed derived pyrolyzed samples (Figure 2d), the SSAs were recorded to be 180, 115, and 140 $m^2 g^{-1}$ for samples TiO_2/C_P, $Al_2O_3/TiO_2/C_{3DP}$, and $Al_2O_3/TiO_2/Pt/C_{3DP}$ respectively. A relatively higher specific surface area of Pt-deposited sample may be due to the fact that the presence of Pt benefits to create additional mesopores (as shown in the PSD of the inset in Figure 2d), which offers additional surface area and resultingly provides more catalytic active sites.

Figure 3a shows the transmission electron microscopy (TEM) image of NH_2-MIL-125(Ti)-derived TiO_2/C_P. The TiO_2 nanoparticles are distributed in a porous carbon matrix, inheriting a disc-like morphology of the Ti-MOF precursor that can also be seen in the SEM images. When mixed with boehmite paste, NH_2-MIL-125(Ti) was homogeneously distributed within the paste. After pyrolyzing the 3D-printed monoliths, the derived TiO_2/C was enveloped by γ-Al_2O_3 nanoparticles (Figure 3b). High-resolution TEM images confirm that the Ti-oxo clusters are transformed into crystalline TiO_2 nanoparticles. The crystalline phase of TiO_2 is determined by the pyrolysis temperature as well as the surrounding chemical environment.[19,42] In Figure 3c, a polyhedral TiO_2 nanoparticle exhibiting different crystalline phases embedded in a porous carbon matrix can be clearly observed. The lattice spacing of the different phases is averaged to be 0.227 and 0.202 nm, attributed to (101) and (200) planes respectively. In sample $TiO_2/Al_2O_3/Pt/C_{3DP}$ (Figure 3d), individual Pt nanoparticles with size around 1.5 nm located next to a larger TiO_2 nanoparticle are clearly seen. The lattice spacing between planes of TiO_2 is measured to be 0.328 nm, corresponding to (101) plane of anatase phase. Compared with the major lattice spacing of pure anatase (0.352 nm) and pure rutile (0.243 nm), the differences in lattice spacing of these MOF-derived TiO_2 nanoparticles are caused by the in situ-doped N and C derived from the organic linker (NH_2-BDC) of precursor NH_2-MIL-125(Ti).[29,42] This was further confirmed by XPS.

Energy dispersive X-ray analysis (EDX) elemental analysis was also carried out to evaluate the distribution of atomic species. As shown in Figure 3e, in Ti-MOF-derived powder sample TiO_2/C_P, elements including Ti, O, C, and N are homogeneously distributed throughout the sample. It is interesting to observe that in 3D-printed samples such as $Al_2O_3/TiO_2/C_{3DP}$ (Figure 3f), all elements including Al are uniformly distributed with content determined by their relative weight percentages in the sample. In Pt-coated 3D-printed sample $Al_2O_3/TiO_2/Pt/C_{3DP}$, a small amount of Pt can also be observed in Figure 3g.

XPS spectra were recorded to investigate the chemical states of the atomic species in 3D-printed precursors (Figure S6, Supporting Information) and the pyrolyzed monoliths (**Figure 4**). The XPS peaks of Ti 2*p* confirm that Ti^{4+} oxidation state are present in all these samples. It is interesting to note that in the 3D-printed boehmite/MOF paste, after loading Pt, the Ti 2*p* peaks remain unchanged (Figure S6a, Supporting Information), indicating that Ti-MOF is very stable. In pyrolyzed Ti-MOF-derived TiO_2/C_P powder, the Ti 2*p* peaks show higher intensities (Figure 4a), whereas in pyrolyzed 3D-printed

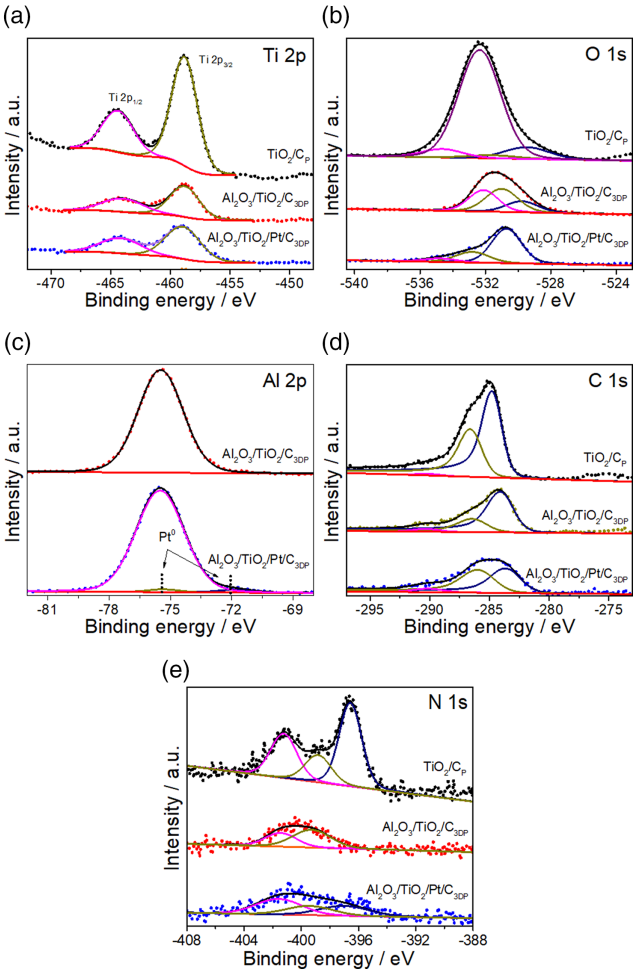

Figure 4. XPS spectra of a) Ti 2*p*, b) O 1*s*, c) Al 2*p*, d) C 1*s*, and e) N 1*s* of the pyrolyzed samples TiO_2/C_P, $Al_2O_3/TiO_2/C_{3DP}$, and $Al_2O_3/TiO_2/Pt/C_{3DP}$.

$Al_2O_3/TiO_2/C_{3DP}$ monoliths, relatively lower intensity of the Ti 2*p* peaks is the reason that TiO_2 nanoparticles are covered with alumina particles.[29,42] The deconvoluted O 1*s* peaks in Ti-MOF precursor (Figure S6b, Supporting Information) are observed at 532.6, 530.5, and 534.8 eV, which are attributed to Ti(IV)—O bond in Ti-oxo cluster and –OH/–COOH group respectively.[23] However, after deposition of Pt, an obvious shift in binding energies is observed. In this sample, the strongest deconvoluted O 1*s* peak is observed at around 532.5 eV, along with the other peaks at 530.1 and 534.7 eV. The change in relative intensity of the deconvoluted O 1*s* peaks clearly indicates that the deposited Pt chemically interacts with O species, forming either Pt—O-like bonds and/or other surface defects.[45,46] In Ti-MOF-derived sample TiO_2/C_P, the main O 1*s* peak (Figure 4b) appearing at 532.4 eV is the signature peak of lattice O in TiO_2. The other two peaks observed at 529.3 and 534.7 eV can be assigned to surface-attached –OH and –COOH functional groups. However, in the presence of alumina in sample $Al_2O_3/TiO_2/C_{3DP}$, the O 1*s* peaks are shifted to the binding energies of 529.7, 531.03, and

532.18 eV respectively.[17,18,51] The presence of Disperal-60, Pural-SB, and acetic acid and a small amount of hydroxypropylmethylcellulose in boehmite/MOF paste precursor contribute to the multiple oxygen species, which upon high-temperature pyrolysis may remain as residues in the form of oxygen-based functional groups, exhibiting higher intensity of –OH/–COOH species compared with the sample TiO_2/C_P. In Pt-deposited sample $Al_2O_3/TiO_2/Pt/C_{3DP}$, the relative intensity of the deconvoluted O 1*s* peaks is changed and the peak positions are shifted to 530.7, 532.8, and 535.2 eV respectively. It clearly indicates that the deposited Pt particles chemically interact strongly with the O species.[46,52]

The oxidation states of the deposited Pt on Ti-MOF precursor were determined by XPS spectra. As shown in Figure S6c, Supporting Information, two main peaks of Pt $4f_{7/2}$ and Pt $4f_{5/2}$ appearing at 69.5 and 72.86 eV respectively represent Pt^0 species, deposited on the Ti-MOF.[45,52] Two small peaks were also observed at 71.6 and 74.9 eV, which can be assigned to Pt $4f_{7/2}$ and Pt $4f_{5/2}$ of Pt^{4+} species.[53,54] However, in 3D-printed MOF-derived composite $Al_2O_3/TiO_2/C_{3DP}$, the binding energy of Al and Pt overlaps and lies in the same region as the signature peak of Al 2*p* is observed at 75.5 eV. In Pt-deposited sample $Al_2O_3/TiO_2/Pt/C_{3DP}$, Al 2*p* peak remains unchanged (Figure 4c). However two additional low intensity peaks can be observed at around 71.9 and 75.5 eV, suggesting the presence of Pt^0 species. It is expected that upon pyrolysis of 3D-printed boehmite/Ti-MOF(Pt) monolith, most of the Pt migrates to TiO_2 at high temperatures and are entrapped only partially in Al_2O_3 but mostly in TiO_2,[55] which is also confirmed by HRTEM and EDX elemental mappings. The presence of Pt in(to)/around TiO_2 was further confirmed by Raman spectra. As shown in Figure S7, Supporting Information, the main vibrational mode $E_g(1)$ of TiO_2 (anatase) appeared at 154 cm^{-1}. A blueshift in $E_g(1)$ compared with pure TiO_2 (144 cm^{-1}) is due to the localized doping of N and C atoms from organic linkers of MOF into TiO_2.[55] The peak appeared at 427 cm^{-1} is assigned to the E_g vibrational mode of rutile TiO_2. In Pt-deposited sample, a small shoulder peak and two new low intensity peaks at around 856.6 and 1082.3 cm^{-1} were observed, which can be attributed to the vibrational modes of metallic Pt^0 and PtO_x species.[44,55]

As shown in Figure 4d, the XPS binding energy peak of sp^2-bonded C=C was observed at 284.8 eV in sample TiO_2/C_P. Two other low-intensity peaks appeared at 286.6 and 290.4 eV that can be assigned to C—O and O—C=O bonds.[42] In 3D-printed boehmite/MOF-derived sample $Al_2O_3/TiO_2/C_{3DP}$, these peaks show a negligible shift indicating that the presence of Al_2O_3 does not change the nature of MOF-derived carbon. However, in Pt-deposited sample, the sp^2 C=C peak was shifted to 283.7 eV, and the C–O peak at 286.0 V was more prominent, which clearly suggests that the deposited Pt atoms are chemically bonded, forming Pt—C and Pt—O like bonds and consequently creating additional surface defects.[47,52,56]

The deconvoluted N 1*s* XPS peaks in precursor Ti-MOF and Pt-deposited Ti-MOF are shown in Figure S8, Supporting Information. The main peak that appeared at 399.3 eV is attributed to the Ti—NH_2 bonds. In Pt-deposited sample, this peak is suppressed and a stronger peak is observed at 396.8 eV, clearly indicating that the Pt atoms attract the electrons from the lone pair of NH_2, forming Pt—N bonds.[53] In sample TiO_2/C_P derived from Ti-MOF (NH_2-MIL-125), N 1*s* spectra (Figure 4e) were deconvoluted into three peaks. The main peak appeared at 396.0 eV can be assigned to Ti—N bonds. The other two low-intensity peaks at 398.9 and 401.3 eV represent pyridinic N and quaternary pyrrolic N atoms in porous carbon matrix derived from organic linker NH_2-BDC in Ti-MOF.[29,42] It is interesting to observe that in 3D-printed boehmite/MOF-derived samples $Al_2O_3/TiO_2/C_{3DP}$, no peak at 396.0 eV is observed. This may be due to the fact that the surface of MOF-derived TiO_2 nanoparticles is encapsulated by a large amount of Al_2O_3, which makes XPS difficult to detect these bonds since XPS is basically a surface technique which normally detects only the surface or near surface of the samples. However, in Pt-deposited 3D-printed sample, this peak appeared at 396.9 eV. The appearance of this peak (in the presence of γ-Al_2O_3) with a shift to higher binding energy compared with TiO_2/C_P sample (396.0 eV) confirms that the Pt atoms do form Pt—N bonds with –NH_2 functional groups in Ti-MOF by attracting more electrons due to their high positive charge.[57–59]

The optical properties of the as-synthesized 3D-printed monoliths were recorded by UV–vis absorption spectra. The absorption band of Ti-MOF (NH_2-MIL-125) appeared at 491 nm.[23,27] In Pt-deposited NH_2-MIL-125 sample, the absorption band was redshifted to 517 nm (Figure S9, Supporting Information), which clearly indicates that the absorption of visible light is improved due to the Pt atoms deposited via ALD being chemically coordinated with the –NH_2 functional groups.[53] Upon pyrolysis of 3D-printed samples, boehmite/Ti-MOF is transformed into Al_2O_3, TiO_2, and carbon composite. The UV–vis absorption spectra (**Figure 5**a) and bandgap energy of the pyrolyzed composites from Tauc plots (Figure 5b) are calculated to be 2.6, 3.0, and 2.9 eV for samples TiO_2/C_P, $Al_2O_3/TiO_2/C_{3DP}$, and $Al_2O_3/TiO_2/Pt/C_{3DP}$ respectively. The bandgap energy of the pristine γ-Al_2O_3 is estimated to be 3.8 eV.

The photocatalytic performance of the Ti-MOF derived and 3D-printed boehmite/Ti-MOF-derived samples for photocatalytic hydrogen (H_2) evolution by water splitting under UV–vis light was tested. A 285 nm cutoff filter was used, and methanol was added as hole scavenger. As shown in **Figure 6**a, the photocatalytic H_2 evolution performance of Ti-MOF-derived powder sample TiO_2/C_P and 3D-printed samples $Al_2O_3/TiO_2/C_{3DP}$ and $Al_2O_3/TiO_2/Pt/C_{3DP}$ all increases with reaction time

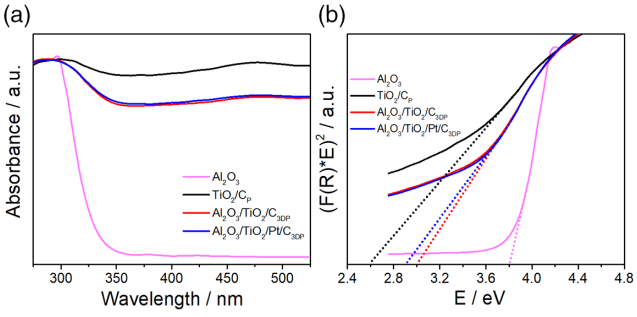

Figure 5. a) UV–vis absorption spectra and b) Tauc plots of pristine γ-Al_2O_3, Ti-MOF-derived TiO_2/C_P, and 3D-printed boehmite/Ti-MOF-derived $Al_2O_3/TiO_2/C_{3DP}$ and $Al_2O_3/TiO_2/Pt/C_{3DP}$.

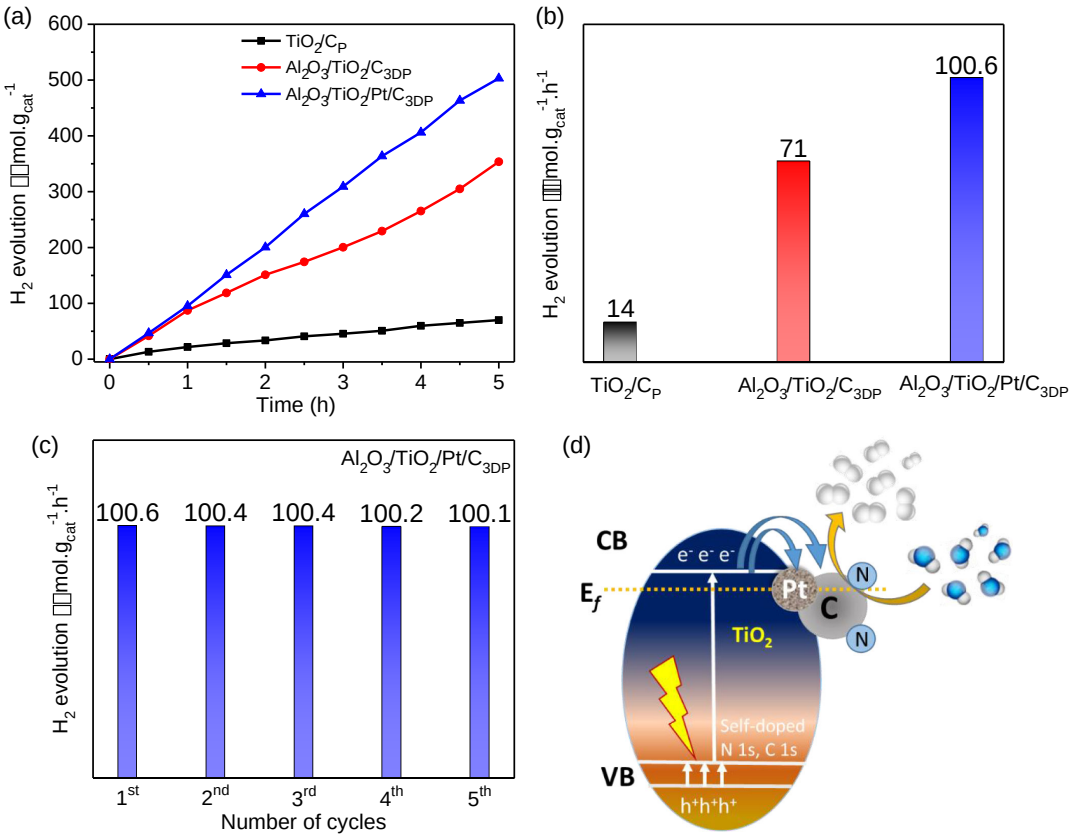

Figure 6. a) Photocatalytic H_2 evolution under UV–vis light for 5 h. b) Photocatalytic activity of TiO_2/C_P (black), $Al_2O_3/TiO_2/C_{3DP}$ (red), and $Al_2O_3/TiO_2/Pt/C_{3DP}$ (blue). c) The recyclability of best-performing sample $Al_2O_3/TiO_2/Pt/C_{3DP}$. d) Schematics illustration of the proposed band structure of active photocatalyst in sample $Al_2O_3/TiO_2/Pt/C_{3DP}$. Here, Al_2O_3 only acts as a support material.

exposure to UV–vis light, and their photocatalytic activities are 70, 354, and 503 μmol. g_{cat}^{-1} respectively after 5 h reaction. In conventional MOF-derived TiO_2/C_P sample, the powder catalyst is dispersed throughout the whole reactor, whereas the diameter of the window of incident light is 2.27 cm^2. Therefore, not all the dispersed catalysts in a traditional reactor configuration are exposed to the photons of the incident light at the same time, which makes it difficult to precisely determine the actual photocatalytic activity of the catalyst.[35] A significant increase in the photocatalytic activity of the 3D-printed samples compared with TiO_2/C_P powder is due to the fact that the 3D-printed catalyst provides a better and much improved incident light exposure to the photoactive N/C-doped TiO_2 nanoparticles which are uniformly distributed throughout the printed monolith. Actually, all the catalysts in printed monoliths are exposed to the incident light at the same time. As a result, an improved photocatalytic activity is expected. As shown in Figure 6b, samples TiO_2/C_P and 3D-printed pyrolyzed monoliths of $Al_2O_3/TiO_2/C_{3DP}$ and $Al_2O_3/TiO_2/Pt/C_{3DP}$ demonstrated H_2 evolution performance of 14, 71, and 101 μmol. $g_{cat}^{-1}.h^{-1}$ respectively. The highest photocatalytic activity of Pt deposited 3D-printed pyrolyzed monoliths can be attributed to various factors including the N/C doped TiO_2, functionalized porous carbon, and the presence of Pt and PtO_x nanoparticles which provide additional active sites.[45,46,56] In these derived samples, photocatalytically active species are N/C-doped TiO_2 nanoparticles and Pt/PtO_x species. A detailed mechanism of photocatalytic H_2 evolution under UV–vis light is discussed in our recently published studies.[19,42,50] As mentioned earlier, this study is a proof of the concept that 3D-printed monoliths can provide a novel method to improve the photocatalytic performance of the materials.

Briefly, when UV–vis light is irradiated and hit on the TiO_2-based catalyst, electrons and holes are generated in anatase and rutile phases of TiO_2 nanoparticles. Since the bandgap energy of γ-Al_2O_3 is very large, and the derived TiO_2 nanoparticles are embedded inside a porous carbon matrix derived from organic linker, therefore, it is less likely that a heterojunction is formed between TiO_2 and Al_2O_3. However, the presence of γ-Al_2O_3 as a support material may help to suppress the charge recombination which results in improvement of the photocatalytic activity of these composite materials. The self-doping of C and N species from organic linker (NH_2–BDC) into TiO_2 during pyrolysis at high temperature in our recent studies[19,42] as well as Pt as a cocatalyst in this study primarily contributes to the enhanced photocatalytic activity. The photogenerated electrons (e^-) in anatase and rutile TiO_2 jump to their respective conduction bands, leaving the holes (h^+) behind in the valence bands. Due to the type-II staggered energy bands (band off-set of 0.4 eV) between anatase and rutile phases of TiO_2, photogenerated electrons migrate to the conduction band of the anatase

phase while the holes migrate to the valence band of the rutile phase. This accumulation of holes and electrons in different phases reduces the charge recombination, which resultingly enhances the photocatalytic activity compared with pure anatase and/or rutile TiO_2.[15,51,60] As confirmed by PXRD, Raman, and XPS spectra, in Ti-MOF-derived N/C-doped TiO_2/C_P and pyrolyzed 3D-printed boehmite/Ti-MOF derived monolith $Al_2O_3/TiO_2/C_{3DP}$, anatase and rutile phases coexist, forming a phase junction.[42,43] In these samples, the photogenerated electrons migrate from the conduction band of rutile phase to the conduction band of anatase phase, whereas the photogenerated holes migrate from the valence band of anatase to the rutile phase. Due to the presence of nitrogen-functionalized porous carbon matrix (9.7 wt%) from organic linker (NH_2-BDC) of Ti-MOF, these photoelectrons also migrate to this carbon, resulting in the minimization of the charge recombination.[50] The photocatalytic reduction reaction takes place at the electron-rich conduction band of anatase phase, which acts as an active site for half reaction, reducing the water molecules into H_2, while the other half reaction of oxidation (in the presence of MeOH) is accommodated by the photogenerated holes in the valence band of rutile phase.[16,20,51] However, in Pt-deposited 3D-printed pyrolyzed monolith $Al_2O_3/TO_2/Pt/C_{3DP}$, only anatase phase is observed by PXRD.[43,45,52,55] This may be due to the deposition of heavy Pt atoms into Ti-MOF, and the phase transformation from anatase to rutile does not take place at 750 °C.[43] Although only anatase phase of TiO_2 is present in 3D-printed pyrolyzed $Al_2O_3/TiO_2/Pt/C_{3DP}$, the uniformly distributed Pt/PtO_x species (calculated to be 0.55 wt% via TGA) provide additional cocatalytic active sites for photocatalytic H_2 evolution reaction. Synergistically, other parameters including high BET surface area, N-functionalized porous carbon, and the presence of γ-Al_2O_3 enable the enhanced accessibility to the photocatalytic active sites; consequently, the printed samples $Al_2O_3/TO_2/C_{3DP}$ and $Al_2O_3/TO_2/Pt/C_{3DP}$ monoliths display much improved photocatalytic performance in H_2 evolution than TiO_2/C_P powder.

The recyclability and the structural stability of the best-performing sample $Al_2O_3/TiO_2/Pt/C_{3DP}$ was also evaluated. As shown in Figure 6c, the photocatalytic H_2 activity almost remains stable and unchanged after five successive photocatalytic performance cycles, each of 5 h. Throughout the reaction process, the structure and morphology of the catalysts also remain unchanged. XRD patterns of the used catalysts $Al_2O_3/TiO_2/C_{3DP}$ and $Al_2O_3/TiO_2/Pt/C_{3DP}$ are the same as that of catalysts prior to the reaction (Figure S10, Supporting Information). Moreover, the optical image (Figure S11a, Supporting Information) confirms that the mechanical stability of the photocatalysts is not sacrificed in water/methanol solution and the overall geometry of the monolith is largely stable. The SEM image (Figure S11b, Supporting Information) further confirms that the disc-like morphology of Ti-MOF-derived photocatalyst embedded in Al_2O_3 is still preserved after the reaction. The benefits of these 3D-printed photocatalysts may offer that the separation of the catalyst from the leftover reaction solution is very easy and no trivial separation processes with excess solvents are needed. Furthermore, by changing from powdery to shaped catalyst, these 3D-printed MOF derivatives offer freedom of customizing the microstructure of the printed monoliths to be fitted to the designed reactor-specific shapes. In addition, the potential change of the use of 3D-printed catalysts from batch or semi-batch setup to continuous flow processes is another advantage. All these suggest that 3D-printed photocatalysts can offer a practical available solution to improve the catalytic performance as well as scaling up of the use of catalyst. For MOF-derived photocatalysts, the catalytic activity can be further improved by optimizing the synthesis parameters such as better shape and size of the printed monoliths (to overcome diffusion limitations that might negatively influence the reaction), controlling over the pyrolysis temperature and tuning gaseous atmosphere. Moreover, increasing and optimizing the content of MOFs in the boehmite/MOF paste precursor to maximize the amount of active catalyst in 3D-printed monoliths can also significantly improve the photocatalytic performance.

3. Conclusion

Ti-MOF NH_2-MIL-125, mixed with boehmite dispersal, was 3D printed by DIW technique followed by Pt deposition using atomic layer deposition. The 3D-printed monoliths were pyrolyzed at 750 °C under Ar atmosphere and the resulting 3D-printed samples were evaluated for photocatalytic H_2 evolution under UV–vis light. As a proof of concept, this study demonstrates that the 3D-printed photocatalytic monoliths exhibit 5 times higher H_2 evolution performance compared with the powder samples due to the better interaction between incident light and the printed catalyst as a maximum amount of catalyst can be exposed to the incident photons. Moreover, the uniformly distributed Pt/PtO_x species, deposited by ALD, provide additional cocatalytic active sites to improve 30% of the H_2 evolution activities compared with Pt-free 3D-printed monoliths. Additionally, N-functionalized porous carbon, high BET surface area, and the presence of porous Al_2O_3 synergistically enhance the accessibility to the photocatalytic active sites. Consequently, the 3D-printed samples $Al_2O_3/TO_2/C_{3DP}$ and $Al_2O_3/TO_2/Pt/C_{3DP}$ monoliths display much improved photocatalytic performance in H_2 evolution than TiO_2/C_P powder.

4. Experimental Section

Synthesis of NH_2-MIL-125(Ti) Powder: To scale up the synthesis of Ti-MOF, NH_2-MIL-125, 6.875 g (38 mmol) of 2-aminoterephthalic acid (NH_2-BDC) was dissolved in 100 mL of dimethylformamide (DMF) and 25 mL methanol (MeOH) mixed solvent. Then, 9.01 mL (26.5 mmol) $Ti(OBu)_4$ was slowly added, followed by the addition of 0.5 mL water, and constantly stirred in an oil bath at 120 °C for 42 h. Yellow colored precipitates were collected by centrifugation. To remove the organic ligand species, the precipitate was washed twice with DMF and then several times with MeOH for solvent exchange. The obtained NH_2-MIL-125(Ti) was dried in air at 70 °C overnight.

Preparation of Boehmite/Ti-MOF Paste and 3D Printing: Following a published procedure,[38] boehmite paste with Disperal-60 and Pural-SB (Sasol Germany GmbH) in a mass ratio of 2.3:1 were mixed with acetic acid (pH = 3, Sigma-Aldrich) to obtain a paste with the solid content of 65 wt%. For the preparation of a mixed paste containing Ti-MOF, the boehmites Disperal–60 and Pural–SB (in the same mass ratio as mentioned before) were mixed with the dried NH_2-MIL-125(Ti) powder in an overall mass ratio of 1.6:0.7:1. The liquid share in the paste was 45 wt%, consisting of acetic acid (pH = 3) and 1 wt%

hydroxypropylmethylcellulose solution in water (Methocel 311, Dow Wolff Cellulosis) in a mass ratio of 1:1.2.

For the DIW printing, a self-constructed printer was used, where the paste was filled in a 2 mL syringe and extruded through a nozzle with a diameter of 0.51 mm. The shapes of 3D-printed monoliths had an overall infill of 40% and a targeted layer height of 0.4 mm. The printed structures were dried overnight on the print bed prior to pyrolysis at high temperatures.

Atomic Layer Deposition (ALD) of Pt: The deposition of Pt on the as-printed boehmite/Ti-MOF monoliths was realized via a commercially available ALD reactor (Savannah S200, UltraTech). Approximately, 50 mg of the pristine MOF powder or 3D-printed boehmite/Ti-MOF monolith was loaded into a standard powder sample holder and held at 150 °C for 2 h to adapt to the process temperature. Argon (Ar) was used as carrier and process gas to introduce the Pt precursor species (5 sccm) and for purging steps (20 sccm of Ar gas). Trimethyl (methylcyclopentadienyl)platinum (IV) ($Me_3PtCpMe$) inside an ALD precursor cylinder was heated to 75 °C prior to the loading experiment. The ALD process was performed at 150 °C with a standard pulse sequence of t_1–t_2–t_3, where precursor pulse time t_1 was 0.015 s, exposure time t_2 was 300 s, and Ar purge time t_3 was 180 s and repeated 50 times. After Pt deposition into the Ti-MOF powder or 3D-printed monoliths, the deposited samples were further purged for several hours to ensure the removal of excess $Me_3PtCpMe$ or any other side products.

Pyrolysis of 3D-Printed Monoliths: The Ti-MOF and the 3D-printed boehmite/Ti-MOF-derived composites were synthesized by one-step direct pyrolysis of respective samples at 750 °C under Ar atmosphere. For that, precursor materials were loaded in an alumina boat and placed in the center of a tube furnace. The heating rate and dwell time of the furnace were set to 5 °C min^{-1} and 2 h, respectively. Prior to the pyrolysis, the quartz tube was purged with Ar gas for 60 min to remove oxygen. The pyrolyzed samples were named as TiO_2/C_P, $Al_2O_3/TiO_2/C_{3DP}$, and $Al_2O_3/TiO_2/Pt/C_{3DP}$. (Here, P stands for powder sample, while 3DP refers to 3D-printed sample.)

Material Characterizations: PXRD patterns of precursor and their derived composites were performed by Rigaku Miniflex. The microscopic images were taken with a MZ8 from Leica that was equipped with a MicroCam II (Bresser). Analysis of the respective images was carried out using ImageJ software. The morphologies of the samples were determined by the images taken by JEOL JSM-7500F field-emission scanning electron microscope coupled with EDX INCA System (software) with 50 mm^2 X-MAX detector from Oxford Instruments. For TEM, samples were applied to glow-discharged C-Flat 1.2/1.3 4C grids (Protochips). Micrographs were acquired at room temperature on a 300 kV Titan Krios electron microscope equipped with a Falcon 3 detector (Thermo Scientific) and a Cs corrector (CEOS). TGA measurements of as-prepared samples, prior to pyrolyzation, were carried out on a TGA Q5000 from TA Instruments under synthetic air with a heating ramp of 10 °C min^{-1}. TGA of derived composites was measured using *Mettler Toledo* TGA/STA 409 PC apparatus under synthetic airflow with a heating ramp of 10 °C min^{-1}. Raman spectra were recorded by Renishaw inVia Reflex Raman System RL532C, Class 3B. The surface chemical analysis was obtained by Kratos Axis Ultra DLD spectrometer with a monochromated Al Kα X-ray source operating at 168 W (12 mA × 14 kV). To calculate the bandgap energies of the nanocomposites, UV–vis absorption spectra were recorded by ThermoScientific Evolution 200 spectrophotometer. For the measurement of BET surface area and the pore PSDs from the N_2 sorption at 77 K, *Quantachrome* autosorb iQ2 ASiQwin equipped with a micropore port (1×10^{-5} bar) was employed. Before the N_2 gas sorption analysis, all the samples were degassed for 6 h at 150 °C under vacuum. The PSD of all the samples was calculated from the adsorption branch using nonlocal density functional theory (NLDFT) method.

Photocatalytic hydrogen (H_2) evolution reactions were performed in a custom-made Pyrex-glass reactor under 500 W Xe/Hg lamp (66 983, Newport). To analyze the evolved gases in headspace, a gas chromatograph (CP 9001, Chrompack), a KSLA gas pump, and the light source were employed. The photocatalytic reactor consisting of a total volume of 42.1 mL (17.1 mL headspace, 2 mL dilution volume) was equipped with a water jacket to precisely control the temperature. In the experiment, either Ti-MOF-derived powder or 3D-printed monoliths were suspended in the photocatalytic reactor with 7.5 mL CH_3OH and 17.5 mL H_2O. The reactor was purged by Ar gas (30 mL min^{-1}) for 30 min to completely deoxygenate the system prior to the reaction and the reactor temperature was set at 30 °C. After complete deoxygenation of the reactor, the UV–vis light illumination was applied, and the reaction products were analyzed by means of the gas chromatography analysis.

Supporting Information

Supporting Information is available from the Wiley Online Library or from the author.

Acknowledgements

M.Z.H. and P.F.G. contributed equally to this work. The authors gratefully acknowledge TUM Innovation Network Artificial Intelligence in Material Science (ARTEMIS), Bayerische Forschungsstiftung (BFS), and Royal Society (IEC\NSFC\201121) for financial support.

Conflict of Interest

The authors declare no conflict of interest.

Data Availability Statement

Research data are not shared.

Keywords

hydrogen generation, metal–organic frameworks, photocatalysis, TiO_2, 3D printing

Received: June 20, 2022
Revised: July 17, 2022
Published online:

[1] W. Gao, S. Liang, R. Wang, Q. Jiang, Y. Zhang, Q. Zheng, B. Xie, C. Y. Toe, X. Zhu, J. Wang, L. Huang, Y. Gao, Z. Wang, C. Jo, Q. Wang, L. Wang, Y. Liu, B. Louis, J. Scott, A.-C. Roger, R. Amal, H. He, S.-E. Park, *Chem. Soc. Rev.* **2020**, *49*, 8584.
[2] R. N. E. Huaman, T. X. Jun, *Renewable Sustainable Energy Rev.* **2014**, *31*, 368.
[3] S. Sun, H. Sun, P. T. Williams, C. Wu, *Sustainable Energy Fuels* **2021**, *5*, 4546.
[4] R. D. Tentu, S. Basu, *Curr. Opin. Electrochem.* **2017**, *5*, 56.
[5] S. Cao, L. Piao, X. Chen, *Trends Chem.* **2020**, *2*, 57.
[6] L. Yuan, C. Han, M.-Q. Yang, Y.-J. Xu, *Int. Rev. Phys. Chem.* **2016**, *35*, 1.
[7] I. P. Jain, *Int. J. Hydrogen Energy* **2009**, *34*, 7368.
[8] L. Barelli, G. Bidini, F. Gallorini, S. Servili, *Energy* **2008**, *33*, 554.
[9] M. Kayfeci, A. Keçebaş, M. Bayat, in *Solar Hydrogen Production* (Eds: F. Calise, M. D. D'Accadia, M. Santarelli, A. Lanzini, D. Ferrero), Academic Press, United Kingdom **2019**, p. 45.
[10] Z. Huang, Z. Yang, Q. Jia, N. Wang, Y. Zhu, Y. Xia, *Nanoscale* **2022**, *14*, 4726.
[11] X. Zhang, Z. Chen, Y. Luo, X. Han, Q. Jiang, T. Zhou, H. Yang, J. Hu, *J. Hazard. Mater.* **2021**, *405*, 124128.
[12] Z. Huang, Z. Yang, M. Z. Hussain, B. Chen, Q. Jia, Y. Zhu, Y. Xia, *Electrochim. Acta* **2020**, *330*, 135335.
[13] J. Low, J. Yu, M. Jaroniec, S. Wageh, A. A. Al-Ghamdi, *Adv. Mater.* **2017**, *29*, 1601694.

[14] C. Di Valentin, E. Finazzi, G. Pacchioni, A. Selloni, S. Livraghi, M. C. Paganini, E. Giamello, *Chem. Phys.* **2007**, *339*, 44.
[15] N. Rahimi, R. A. Pax, E. M. Gray, *Prog. Solid State Chem.* **2016**, *44*, 86.
[16] X. Chen, C. Burda, *J. Am. Chem. Soc.* **2008**, *130*, 5018.
[17] S. G. Kumar, L. G. Devi, *J. Phys. Chem. A* **2011**, *115*, 13211.
[18] R. Asahi, T. Morikawa, T. Ohwaki, K. Aoki, Y. Taga, *Science* **2001**, *293*, 269.
[19] M. Z. Hussain, B. van der Linden, Z. Yang, Q. Jia, H. Chang, R. A. Fischer, F. Kapteijn, Y. Zhu, Y. Xia, *J. Mater. Chem. A* **2021**, *9*, 4103.
[20] D. O. Scanlon, C. W. Dunnill, J. Buckeridge, S. A. Shevlin, A. J. Logsdail, S. M. Woodley, C. R. A. Catlow, M. J. Powell, R. G. Palgrave, I. P. Parkin, G. W. Watson, T. W. Keal, P. Sherwood, A. Walsh, A. A. Sokol, *Nat. Mater.* **2013**, *12*, 798.
[21] H. Li, M. Eddaoudi, M. O'Keeffe, O. M. Yaghi, *Nature* **1999**, *402*, 276.
[22] H. Zhou, J. R. Long, O. M. Yaghi, *Chem. Rev.* **2012**, *112*, 673.
[23] P. Karthik, A. R. M. Shaheer, A. Vinu, B. Neppolian, *Small* **2020**, *16*, 1902990.
[24] F. Song, W. Li, Y. Sun, *Inorganics* **2017**, *5*, 40.
[25] H. L. Nguyen, *Sol. RRL* **2021**, *5*, 2100198.
[26] K. Meyer, M. Ranocchiari, J. A. van Bokhoven, *Energy Environ. Sci.* **2015**, *8*, 1923.
[27] M. A. Nasalevich, M. van der Veen, F. Kapteijn, J. Gascon, *CrystEngComm* **2014**, *16*, 4919.
[28] H. Luo, Z. Zeng, G. Zeng, C. Zhang, R. Xiao, D. Huang, C. Lai, M. Cheng, W. Wang, W. Xiong, Y. Yang, L. Qin, C. Zhou, H. Wang, Y. Zhou, S. Tian, *Chem. Eng. J.* **2020**, *383*, 123196.
[29] M. Z. Hussain, M. Bahri, W. R. Heinz, Q. Jia, O. Ersen, T. Kratky, R. A. Fischer, Y. Zhu, Y. Xia, *Microporous Mesoporous Mater.* **2021**, *316*, 110957.
[30] S. V. Dummert, H. Saini, M. Z. Hussain, K. Yadava, K. Jayaramulu, A. Casini, R. A. Fischer, *Chem. Soc. Rev.* **2022**, *51*, 5175.
[31] M. Z. Hussain, Z. Yang, Z. Huang, Q. Jia, Y. Zhu, Y. Xia, *Adv. Sci.* **2021**, *8*, 2100625.
[32] W. Xia, A. Mahmood, R. Zou, Q. Xu, *Energy Environ. Sci.* **2015**, *8*, 1837.
[33] L. Oar-Arteta, T. Wezendonk, X. Sun, F. Kapteijn, J. Gascon, *Mater. Chem. Front.* **2017**, *1*, 1709.
[34] Z. Huang, Z. Yang, M. Z. Hussain, Q. Jia, Y. Zhu, Y. Xia, *J. Mater. Sci. Technol.* **2021**, *84*, 76.
[35] N. Serpone, A. V. Emeline, V. K. Ryabchuk, V. N. Kuznetsov, Y. M. Artem'ev, S. Horikoshi, *ACS Energy Lett.* **2016**, *1*, 931.
[36] C.-Y. Lee, A. C. Taylor, A. Nattestad, S. Beirne, G. G. Wallace, *Joule* **2019**, *3*, 1835.
[37] B. Yao, S. Chandrasekaran, J. Zhang, W. Xiao, F. Qian, C. Zhu, E. B. Duoss, C. M. Spadaccini, M. A. Worsley, Y. Li, *Joule* **2019**, *3*, 459.
[38] T. Ludwig, J. von Seckendorff, C. Troll, R. Fischer, M. Tonigold, B. Rieger, O. Hinrichsen, *Chem. Ing. Tech.* **2018**, *90*, 703.
[39] Z. Lyu, G. J. H. Lim, R. Guo, Z. Kou, T. Wang, C. Guan, J. Ding, W. Chen, J. Wang, *Adv. Func. Mater.* **2019**, *29*, 1806658.
[40] B. Kraushaar-Czarnetzki, S. Peter Müller, in *Synthesis of Solid Catalysts* (Eds: K. P. de Jong), Wiley-VCH Verlag, Weinheim, Germany **2009**, p. 173.
[41] Y. Chen, O. Ola, G. Liu, L. Han, M. Z. Hussain, K. Thummavichai, J. Wen, L. Zhang, N. Wang, Y. Xia, Y. Zhu, *J. Eur. Ceram. Soc.* **2021**, *41*, 3970.
[42] M. Z. Hussain, Z. Yang, B. V. D. Linden, Z. Huang, Q. Jia, E. Cerrato, R. A. Fischer, F. Kapteijn, Y. Zhu, Y. Xia, *J. Energy Chem.* **2021**, *57*, 485.
[43] M. Bouslama, M. C. Amamra, Z. Jia, M. Ben Amar, K. Chhor, O. Brinza, M. Abderrabba, J. L. Vignes, A. Kanaev, *ACS Catal.* **2012**, *2*, 1884.
[44] T. Huizinga, J. Van Grondelle, R. Prins, *Appl. Catal.* **1984**, *10*, 199.
[45] J. Yu, L. Qi, M. Jaroniec, *J. Phys. Chem. C* **2010**, *114*, 13118.
[46] Y. Zhang, H. Hu, X. Huang, Y. Bi, *J. Mater. Chem. A* **2019**, *7*, 5938.
[47] A. C. Ferrari, J. Robertson, *Phys. Rev. B* **2000**, *61*, 14095.
[48] A. Y. Lee, K. Yang, N. D. Anh, C. Park, S. M. Lee, T. G. Lee, M. S. Jeong, *Appl. Surf. Sci.* **2021**, *536*, 147990.
[49] B. N. Bhadra, A. Vinu, C. Serre, S. H. Jhung, *Mater. Today* **2019**, *25*, 88.
[50] M. Z. Hussain, Z. Yang, A. M. E. Khalil, S. Hussain, S. U. Awan, Q. Jia, R. A. Fischer, Y. Zhu, Y. Xia, *J. Mater. Sci. Technol.* **2022**, *101*, 49.
[51] J. Schneider, M. Matsuoka, M. Takeuchi, J. Zhang, Y. Horiuchi, M. Anpo, D. W. Bahnemann, *Chem. Rev.* **2014**, *114*, 9919.
[52] P. Wang, S. Zhan, Y. Xia, S. Ma, Q. Zhou, Y. Li, *Appl. Catal., B* **2017**, *207*, 335.
[53] Y. Zhong, R. Wang, X. Wang, Z. Lin, G. Jiang, M. Yang, D. Xu, *Front. Chem.* **2020**, *8*, 660.
[54] J. Wang, A. S. Cherevan, C. Hannecart, S. Naghdi, S. P. Nandan, T. Gupta, D. Eder, *Appl. Catal., B* **2021**, *283*, 119626.
[55] L. Chen, L. Kovarik, J. Szanyi, *ACS Catal.* **2021**, *11*, 12058.
[56] Q. Xiang, J. Yu, M. Jaroniec, *Nanoscale* **2011**, *3*, 3670.
[57] Y. Hu, Y. Qu, Y. Zhou, Z. Wang, H. Wang, B. Yang, Z. Yu, Y. Wu, *Chem. Eng. J.* **2021**, *412*, 128749.
[58] H. Sun, R. Ullah, S. Chong, H. M. Ang, M. O. Tadé, S. Wang, *Appl. Catal., B* **2011**, *108–109*, 127.
[59] Q. Shi, C. Zhu, M. H. Engelhard, D. Du, Y. Lin, *RSC Adv.* **2017**, *7*, 6303.
[60] R. Su, R. Bechstein, L. Sø, R. T. Vang, M. Sillassen, B. Esbjörnsson, A. Palmqvist, F. Besenbacher, *J. Phys. Chem. C* **2011**, *115*, 24287.